A fast yet force-effective mode of collective cell migration on aligned fibers due to rapid stabilization of contractile forces

Authors: Amrit Bagchi[1], Bapi Sarker[1], Jialiang Zhang[2], Marcus Foston[2], Amit Pathak[1,*]

Affiliations: [1]*Department of Mechanical Engineering & Materials Science,* [2]*Department of Energy, Environmental & Chemical Engineering, Washington University, St. Louis*

*To whom correspondence should be addressed:
Amit Pathak, Ph.D.
One Brookings Dr., CB 1185, Saint Louis, MO 63130
Ph: (314) 935-7585; Email: pathaka@wustl.edu

Abstract:

Cell collectives use aligned extracellular matrix fibers for directed migration in development, regeneration, and cancer metastasis. However, it remains unknown whether fibers serve as active conduits for spatial propagation of cellular mechanotransduction leading to directed collective cell migration. In this work, we developed soft hydrogels coated with magnetically aligned collagen fibers and studied migration of defined epithelial clusters. We report that epithelial (MCF10A) cell clusters adhered to soft substrates with aligned collagen fibers (AF) migrate faster with much lesser traction forces, compared to those on uniform fibers (UF). Fiber alignment causes motility and force transmission deeper into the monolayer, leading to polarized cell flocking, compared to migration on UF where cellular jamming occurs. Using a motor-clutch model, we explain that force-effective fast migration phenotype occurs due to faster stabilization of cellular contractile forces enabled by aligned ligand connectivity. As a result, cells migrate faster with lesser effort, thereby revealing that aligned matrix topographies may help conserve energy for cell migration in fundamental biological processes such as wound repair and tumor invasion.

Significance statement:

Cellular forces are critical for their collective migration on matrices of various stiffness and topographies. While cells can align collagen fibers during migration, it remains unknown whether such force requirement changes with pre-aligned fibers. On soft surfaces with aligned collagen fibers, we discovered a new mode of fast collective cell migration that requires drastically lower traction forces, compared to surfaces without aligned fibers. Through monolayer stress microscopy calculations and a motor-clutch model, we further discovered that this novel mode of “fast and force-effective” collective cell migration is achieved by rapid stabilization of cellular contractile forces. Although high traction forces have conventionally been associated with fast cell migration, our findings show that aligned fibers relax that force requirement via contractility stabilization.

Main Text:

Directed collective cell migration is ubiquitous in fundamental processes like organ development and regeneration (*1*), (*2*). However, physical or biochemical mechanisms that dictate mesoscopic order across supra-cellular length scales are not well understood. Mechanistically, large-scale propagation of mechanical signals leading to directionally cooperative behavior has been recognized, but not yet elucidated. Recently, collective cells undergoing directional migration on substrates having gradients in stiffness (durotaxis) have shown to utilize long range force propagation (*3*) aided via underlying substrate, motivating a hypothesis that efficient signal transduction could be a key component in explaining directional migration. Thus, it is possible that if extracellular force propagation works in coordination with mechanical stress transfer across cell-cell junctions, such cooperation could generate more efficient collective cell migration. This is an intriguing possibility given that force transfer across cellular junctions correlates only to a limited spatial extent in unbiased migration, thereby reducing migration efficiency.

Directional collective migration via contact guidance in the form of aligned extracellular matrix (ECM) fibers is critical in tissue healing and regenerations (*4*)–(*6*) as well as a strong regulator of carcinoma progression (*7*)–(*10*). There have been extensive studies on parallel grooves or adhesive ligands aimed at mimicking this phenomenon in 2D (*11*)–(*14*). While these studies have focused on capturing ligand continuity in a particular direction by uniformly coating ligands along the topography or adhesive strip, the fact that ligands on aligned fibers *in vivo* are connected to each other and can potentially serve as sources of large-scale propagation of mechanical signals has not yet been investigated. This gap in knowledge provides us with an opportunity to test our hypothesis of extra-cellular force propagation via aligned fibers as an adjuvant to mechanical stress transfer across cellular junctions helping cellular cohorts to exhibit directional migration in aligned fibrous microenvironments.

To probe the above hypothesis, we develop an experimental approach where we use aligned collagen-1 fibers as directional cues for cell migration on soft 2D surfaces that mimic physiological stiffness. We first synthesize modified soft polyacrylamide (mod-PA) hydrogels, which enable attachment of tunable collagen fibers, as previously described (*15*). We then incubate these hydrogels in a collagen-1 solution (0.1 mg/ml) and expose to a high-strength magnetic field (11 T) during collagen fibrillogenesis at 4° C (Fig. 1b, Fig. S1a) (*16*). During this process, collagen fibers settle and covalently attach to the gels, with alignment along a desired direction (*15*). Next, using magnetic polydimethyl-siloxane (PDMS) stencils, we micro-patterned rectangular clusters (500 µm wide) of human mammary epithelial cells (MCF-10A) on these aligned collagen-coated mod-PA gels in a manner such that directions of leading edge advancement and collagen alignment are parallel (Fig 1a). We measure the effect of collagen alignment on collective migration by comparing it against uniformly distributed collagen fibers without alignment bias. To achieve uniformly coated collagen surfaces, mod-PA gels were incubated with collagen solution at 37° C, without magnetic field, followed by cell cluster patterning (Fig. 1c, Fig. S1b) (*15*).

Upon removal of the PDMS stencil, rectangular cell clusters expanded symmetrically on both aligned fiber gels (AF) and uniform fiber gels (UF) (Fig. 1 (d, e)). To better understand the large-scale spatiotemporal fluctuations of mechanical patterns within the expanding monolayer, we averaged velocities, tractions, and monolayer stresses across length (y-coordinate), thereby reducing

dimensionality of system to a single spatial dimension (x-axis, which is the also the direction of collagen alignment) and the temporal dimension (Fig. 1 (h-k), 2 (a-d), 3(i-n)). By comparing cell migration trajectories (Fig. 1f-g, Fig. S1c-d), we observed that cell clusters on AF migrated faster (1.8 times) compared to the cells migrating on UF. Additionally, cell clusters migrated more persistently along the x-direction leading to a net higher expansion of the monolayer on AF, indicating that cells were using aligned fibers as directional cues to navigate their migration (Fig S1e). For AF, cell movements were more homogenous with higher velocities at the leading edge penetrating greater depths within the monolayer, compared to a more heterogeneous distribution in UF characterized by outward faster velocities and middle regions with much lesser velocities (Fig. 1h,i). Quantitatively, the spatial velocity autocorrelation function follows a slower spatial decay in AF, confirming that cellular motion is correlated across greater distances when compared to UF (Fig. 1i).

Given the spatial cooperation in migrating cells driven by aligned fibers, we next investigated whether cell movements had differences in temporal heterogeneity across the conditions. We measure this heterogeneity using the four-point susceptibility χ_4, a soft matter physics tool used for measuring the rate of structural rearrangements between any two points in space within a time window. We computed χ_4 from the variance of the self-overlap order parameter (see Methods). While the location of the peak of χ_4 indicates time interval in which cell migration dynamics are highly heterogeneous, the height of the peak denotes the spatial extent of such heterogeneities (*17*). Comparing AF versus UF, there is a distinct shift in χ_4 peak to longer timescales for UF (Fig. 1m), indicating a more jammed state for cells migrating on UF. Additionally, the peak height for UF is higher, indicating larger clusters of jammed cells in UF. According to previous work in inert particulate matter (*18*), (*19*), differences in mutual crowding between the two conditions could be responsible for promoting jamming in one condition over the other. To explore this potential mechanism for the observed jamming differences in AF and UF, we measured cellular areas (Fig. 1n,o) densities (Fig. S1d)and aspect ratios (Fig. 1n, Fig. S1e)) across the two conditions. As shown in figures, cells on UF tended to have a higher area and aspect ratio compared to AF while also having much lesser densities. While cellular morphologies do agree with the notion that cells on UF are in a more jammed state (*20*), it is quite counter-intuitive to find that such a state existed in UF at lesser cellular densities when compared to AF. This is particularly surprising because jamming tends to occur at higher densities in inert systems (*19*), (*21*). This experimental evidence thus helps us to reject a density based jamming hypothesis. For the cells in the x-direction on AF, our analysis suggest a flocking type of migratory phenotype (*22*), (*23*), which is spatially homogenous and temporally dynamic. By contrast, on UF, migration is much more heterogeneous and static. It is possible that these differences in phenotype are a result of homogeneity in ligand orientation on AF and the lack thereof on UF.

Interestingly, for AF alone, there were multiple strain-rate X-waves propagating away from leading edge, coalescing at the middle of the monolayer and then propagating back to the edge (Fig. 1j,k, Fig. 2l,m). This phenomenon was less frequent for UF. Although efficiency of mechanical wave transmission has not been linked to jamming before, the results here do provide evidence to the hypothesis that cell mobilization away from the leading edge is higher and more efficient on AF compared to UF. Interestingly, this transmission takes place across greater number of cell-cell junctions on AF owing to density differences between the two conditions.

Experimental results presented thus far suggest that cell clusters on AF migrate with faster velocities. This unjammed migration phenotype also displays an effective relay of motion from the monolayer front to the rear. By contrast, on UF, cells are slower and jammed with a disrupted transmission of motion. Since motion of a collective cohort of cells depends on the effective transfer of stresses across the monolayer (*24*), and while we see effective transfer of motion in only one of the condition, we sought to compare how well forces were getting transmitted across the cells between the conditions. To this end, we first studied traction force evolution within the monolayer. For AF, tractions in x-direction (T_x) kymographs demonstrated much lower (1/5th) traction magnitudes compared to UF (Fig. 2 a,b). Although direct force measurements have not been reported before, this result is surprising because migration studies on stiff substrates in the past have suggested that cells apply higher forces on aligned topographies (*14*). Interestingly, the traction distribution for both conditions was different. While tractions were evenly distributed across the monolayer width on AF, there were heterogeneities in UF, with higher tractions localized at the leading edges, followed by a steep decrease in middle regions. These differences in traction distribution run parallel to the velocity distribution differences seen between the two conditions.

Since the T_x kymographs hint at differences in force transmission across the monolayer width between the two fiber alignment conditions, we probe this further by measuring force transmission using monolayer stress microscopy (*25*). Although kymographs for monolayer stress component σ_{xx} for both AF and UF (Fig. 2c,d) showed maxima at the monolayer midline, indicating build-up of stress differentials at the monolayer center via cell-cell junctions, the extent of this build-up was different for both conditions. Cells on AF had one-fifth of the built-up stresses compared to UF (Fig. 2c,d). This difference was also reflected in the average strain energy plots, which show that cells on AF transfer one-fifth of the strain energy to the substrate compared to the UF (Fig. 2q). To examine the extent of stress cooperativity within the monolayer, we also calculated the spatial correlation function (*C(R)*) of the average normal stress. As shown in Fig 2(p), cells on AF exhibit slower spatial decay of *C(R)*, indicating that average normal stresses were correlated over greater distances. Interestingly, according to T_y kymographs, cells on AF apply negligible forces in the y-direction, while cells on UF apply much higher forces that are equivalent to forces in x-direction (Fig. S3c-e). These distinct differences in T_y indicate that cells on AF are polarized along the direction of collagen alignment and predominantly pull along the collagen fibers, while cells on UF apply forces isotropically without a directional bias.

Since cellular velocity and stress propagate across the monolayer differently between AF and UF, we next probed the relationship between these two fundamental physical quantities that determine grouped cell behavior. Earlier studies have shown that cells have the tendency to migrate along the direction of minimal shear stress, a phenomenon known as "plithotaxis" (*25*). To check the effect of collagen alignment on plithotaxis, we first rank-ordered the pairs of stress and velocity according to their distances from leading edge into 5 quintiles (Fig. 2g-i). Next, for each quintile, we measured the alignment angle φ between local maximal principal stress orientation and local migration velocity vector orientation. We calculated the cumulative probability distribution of φ for each quintile to assess the extent of alignment between velocity and maximal principal stress. Higher degree of alignment would be associates with a steeper rising curve. In both AF and UF, we observe that moving away from the leading edge causes reduction in alignment between local stress and cellular motion, indicating that plithotaxis is most

160 dominant at the leading edge (Fig. 2r,s). However, for each quintile, AF shows a stronger alignment
161 between stress and velocity (steeper curve) when compared to UF. This indicates that plithotaxis is more
162 dominant in AF at all regions within the monolayer when compared to UF, which supports our hypothesis
163 of an efficient transfer of stresses from front to rear of the migrating monolayer across its cell-cell
164 junctions. This long-distance stress propagation guided by aligned collagen fibers enables a more effective
165 transfer of motion from the leader to the follower population. By contrast, both the front-rear stress
166 propagation and the leader-follower velocity cooperation get disrupted when fibers are uniformly
167 distributed without any preferred orientation.

168 Previously, cytoskeletal fluidization has been shown to regulate dissipation of built-up stresses
169 within cell monolayers for their active expansion (*26*). Here, we measure the extent of fluidization within
170 the monolayer by measuring stress oscillations at the monolayer midline. Multiple stress peaks arise for
171 AF, compared to a single such peak in UF for the entire migration duration (Fig. 2l,m). These periodic built-
172 up and release of stresses at the monolayer midline for AF indicates an efficient long-range stress
173 transmission across cells, a process absent in UF. Additionally, in accordance with previous literature (*26*),
174 these stress oscillations were in a phase quadrature to velocity strain rate oscillations but in phase with
175 cellular area fluctuations (Fig. 2n,o). Given that stresses are more frequently dissipated in AF, it would be
176 indicative of more frequent regulation of cell size, consistent with recent work showing coordination of
177 cell size and stress within a monolayer (*27*). This cell size-stress balancing act could explain why stresses
178 within the monolayer are not allowed to build up, leading to overall lower stresses on AF. On AF, higher
179 frequency of cell shape adaptation results in overall reduction in cell size as stresses are seamlessly
180 transferred across cells. However, on UF, infrequent transfer of stresses leads to stress build-up within
181 the cells, which coincides with increase in cell size.

182 As a confirmation of the above phenotype, we repeated the experiment by further lowering the mod-PA
183 substrate stiffness. We find that cells still migrate faster on AF compared to UF (1.34 times) while applying
184 much lesser forces ($1/4^{th}$) on AF when compared to UF (Fig. S3a,c). We also find that both cellular
185 velocities and stresses are correlated across greater distances in clusters migrating on AF (Fig. S3b,d).
186 Expectedly, we also observed higher spatial extent of plithotaxis in clusters migrating on AF (Fig. S4e-i).

187 Our experimental measurements establish that monolayers use aligned collagen fibers to expand
188 faster while generating lesser contractile tractions and monolayer stresses. Also, we show that these
189 forces are transmitted across greater distances within the cluster. To better understand why fiber
190 alignment leads to faster migration without the need for higher forces, we developed a physical model
191 which incorporates clutch-like cell-ECM interactions in a minimalist framework wherein cell monolayer,
192 collagen fibers, and soft substrate are treated as a collection of elastic springs connected in series (Fig.
193 4a). While UF is modelled as individual ligand springs disconnected from one another, AF is modelled by
194 connecting these ligand springs to each other, depicting ligand connectivity along the direction of
195 migration (Fig. 4b,c).

196 The model predicts a faster cell cluster expansion during its migration over connected ligand
197 springs (compared to the disconnected condition), while generating lesser traction forces on the
198 underlying substrate mesh. Cells within the cluster are also able to fluidize more often when migrating
199 over connected fibers, thus leading to release of build-up stress within the cell cluster. In our model, fiber

connectivity causes engagement of more ligand-substrate bonds as the leading-edge cell node contracts after a protrusion event. This rise in ligand-substrate bonds results in higher load sharing capability amongst the nodes, leading to quicker stabilization of the contracting leading edge. Quicker stabilization further leads to faster subsequent protrusions and overall expansion of the cluster (Fig. 4d,e). Another effect of faster contractility stabilization is reduced retraction of the cell cluster, compared to the disconnected fiber condition, which in turn causes lesser substrate deformation and traction (Fig. 4f,g). As a whole, the faster stabilization of the leading edge on connected fibers causes quicker transfer of stress from the edge to the center, which in turn results in faster stretch-based cell fluidization within the monolayer. However, in case of slower stabilization of cluster edge, the related slower transfer of strains to the center reduces the frequency of fluidization events within the monolayer (Fig. 4h,i).

Given the close agreement between the experiments and model predictions, we conclude that long-range force transmission via connected ligands leads to a more efficient mode of migration in terms of force required to generate migration velocity on matrix conditions that offer higher ligand connectivity. While long-range force transmission as an underlying mechanism for collective directional migration has been alluded to in the past (*3*), our experiments use constant matrix stiffness across conditions, thus keeping stiffness sensitive mechano-transduction pathways within the cells constant and thereby removing the effective contribution of stiffness from directional migration or its effect in long range force transmission. We also speculate that utilizing aligned ECM fibers on 2D substrates gives rise to a quasi-2D mode of contact-guided directional migration, which delineates the role of ligand connectivity as opposed to uniformly coated ligands on micropatterned protein stripes or topographical grooves (*11*), (*13*). Uniform ligand coating leads to ligand continuity but not connectivity, thus restricting matrix mechano-transmission that could take place outside of the cell monolayer. In light of recent evidence of cell division upregulation upon mechanical stretching (*28*), future work could explore how differences in mechanical properties within the monolayer dictates the ease of proliferation-based monolayer fluidization in the presence of ligand connectivity.

227 ## References and Notes:

228 1. A. McMahon, G. T. Reeves, W. Supatto, A. Stathopoulos, Mesoderm migration in Drosophila is a
229 multi-step process requiring FGF signaling and integrin activity. *Development*. ***137***, 2167–2175
230 (2010).

231 2. R. J. Petrie, A. D. Doyle, K. M. Yamada, Random versus directionally persistent cell migration. *Nat.*
232 *Rev. Mol. Cell Biol.* ***10***, 538–549 (2009).

233 3. R. Sunyer *et al.*, Collective cell durotaxis emerges from long-range intercellular force
234 transmission. *Science (80-.).* ***353***, 1157–1161 (2016).

235 4. R. T. Tranquillo, Self-organization of tissue-equivalents: the nature and role of contact guidance.
236 *Biochem. Soc. Symp.* ***65***, 27–42 (1999).

237 5. G. Reig, E. Pulgar, M. L. Concha, Cell migration: from tissue culture to embryos. *Development*.
238 ***141***, 1999–2013 (2014).

239 6. A. Czirok, Endothelial cell motility, coordination and pattern formation during vasculogenesis.
240 *Wiley Interdiscip. Rev. Syst. Biol. Med.* ***5***, 587–602 (2013).

241 7. P. P. Provenzano, D. R. Inman, K. W. Eliceiri, S. M. Trier, P. J. Keely, Contact Guidance Mediated
242 Three-Dimensional Cell Migration is Regulated by Rho/ROCK-Dependent Matrix Reorganization.
243 *Biophys. J.* ***95***, 5374–5384 (2008).

244 8. P. P. Provenzano *et al.*, Collagen density promotes mammary tumor initiation and progression.
245 *BMC Med.* ***6***, 11 (2008).

246 9. P. P. Provenzano, K. W. Eliceiri, J. M. Campbell, D. R. Inman, J. G. White, P. J. Keely, Collagen
247 reorganization at the tumor-stromal interface facilitates local invasion. *BMC Med.* ***4***, 38 (2006).

248 10. M. W. Conklin *et al.*, Aligned collagen is a prognostic signature for survival in human breast
249 carcinoma. *Am. J. Pathol.* ***178***, 1221–1232 (2011).

250 11. S. R. K. Vedula *et al.*, Emerging modes of collective cell migration induced by geometrical
251 constraints. *Proc. Natl. Acad. Sci.* ***109***, 12974–12979 (2012).

252 12. S. R. K. Vedula *et al.*, Epithelial bridges maintain tissue integrity during collective cell migration.
253 *Nat. Mater.* ***13***, 87–96 (2014).

254 13. C. Leclech, D. Gonzalez-Rodriguez, A. Villedieu, T. Lok, A.-M. Déplanche, A. I. Barakat,
255 Topography-induced large-scale antiparallel collective migration in vascular endothelium. *Nat.*
256 *Commun.* ***13***, 2797 (2022).

257 14. J. Park *et al.*, Switch-like enhancement of epithelial-mesenchymal transition by YAP through
258 feedback regulation of WT1 and Rho-family GTPases. *Nat. Commun.* ***10***, 2797 (2019).

259 15. B. Sarker, A. Bagchi, C. Walter, J. Almeida, A. Pathak, Longer collagen fibers trigger multicellular
260 streaming on soft substrates via enhanced forces and cell–cell cooperation. *J. Cell Sci.* ***132***,

261 jcs226753 (2019).

262 16. T. Greeshma *et al.*, Cell contact guidance via sensing anisotropy of network mechanical
263 resistance. *Proc. Natl. Acad. Sci.* ***118***, e2024942118 (2021).

264 17. A. S. Keys, A. R. Abate, S. C. Glotzer, D. J. Durian, Measurement of growing dynamical length
265 scales and prediction of the jamming transition in a granular material. *Nat. Phys.* ***3***, 260–264
266 (2007).

267 18. V. Trappe, V. Prasad, L. Cipelletti, P. N. Segre, D. A. Weitz, Jamming phase diagram for attractive
268 particles. *Nature*. ***411***, 772–775 (2001).

269 19. A. J. Liu, S. R. Nagel, Jamming is not just cool any more. *Nature*. ***396***, 21–22 (1998).

270 20. L. Atia *et al.*, Geometric constraints during epithelial jamming. *Nat. Phys.* ***14***, 613–620 (2018).

271 21. A. J. Liu, S. R. Nagel, The Jamming Transition and the Marginally Jammed Solid. *Annu. Rev.*
272 *Condens. Matter Phys.* ***1***, 347–369 (2010).

273 22. C. Malinverno *et al.*, Endocytic reawakening of motility in jammed epithelia. *Nat. Mater.* ***16***, 587–
274 596 (2017).

275 23. F. Giavazzi *et al.*, Flocking transitions in confluent tissues. *Soft Matter*. ***14***, 3471–3477 (2018).

276 24. D. T. Tambe *et al.*, Collective cell guidance by cooperative intercellular forces. *Nat. Mater.* ***10***,
277 469–475 (2011).

278 25. D. T. Tambe *et al.*, Collective cell guidance by cooperative intercellular forces. *Nat. Mater.* ***10***,
279 469–475 (2011).

280 26. X. Serra-Picamal *et al.*, Mechanical waves during tissue expansion. *Nat. Phys.* ***8***, 628–634 (2012).

281 27. A. Saraswathibhatla, J. Zhang, J. Notbohm, Coordination of contractile tension and cell area
282 changes in an epithelial cell monolayer. *Phys. Rev. E*. ***105***, 24404 (2022).

283 28. S. A. Gudipaty *et al.*, Mechanical stretch triggers rapid epithelial cell division through Piezo1.
284 *Nature*. ***543***, 118–121 (2017).

285

286

287 ## Acknowledgements:

288 The authors acknowledge technical assistance and equipment sharing by Dr. James Quirk for using MRI
289 strength magnet and Professor Vijay Ramani for the use of vacuum filtration and rota-evaporator. This
290 work was supported by the NIH/NIGMS grant R35GM128764 (to AP) and National Science Foundation,
291 Science and Technology Centers, Center for Engineering MechanoBiology grant CMMI:154857 (to AP
292 and MF).

Author Contributions

AB and AP conceived the project and designed study. AB performed experiments and computational modeling, analyzed data, interpreted findings, made figures, and wrote the manuscript. BS, JZ and MF contributed methods and reagents for polyacrylamide gel synthesis. AP edited the manuscript, supervised the project, and acquired funding.

Conflicts of Interest

The authors declare no competing interests.

Data Availability

Source codes used for data analysis and plotting figures are available on reasonable request.

Figures

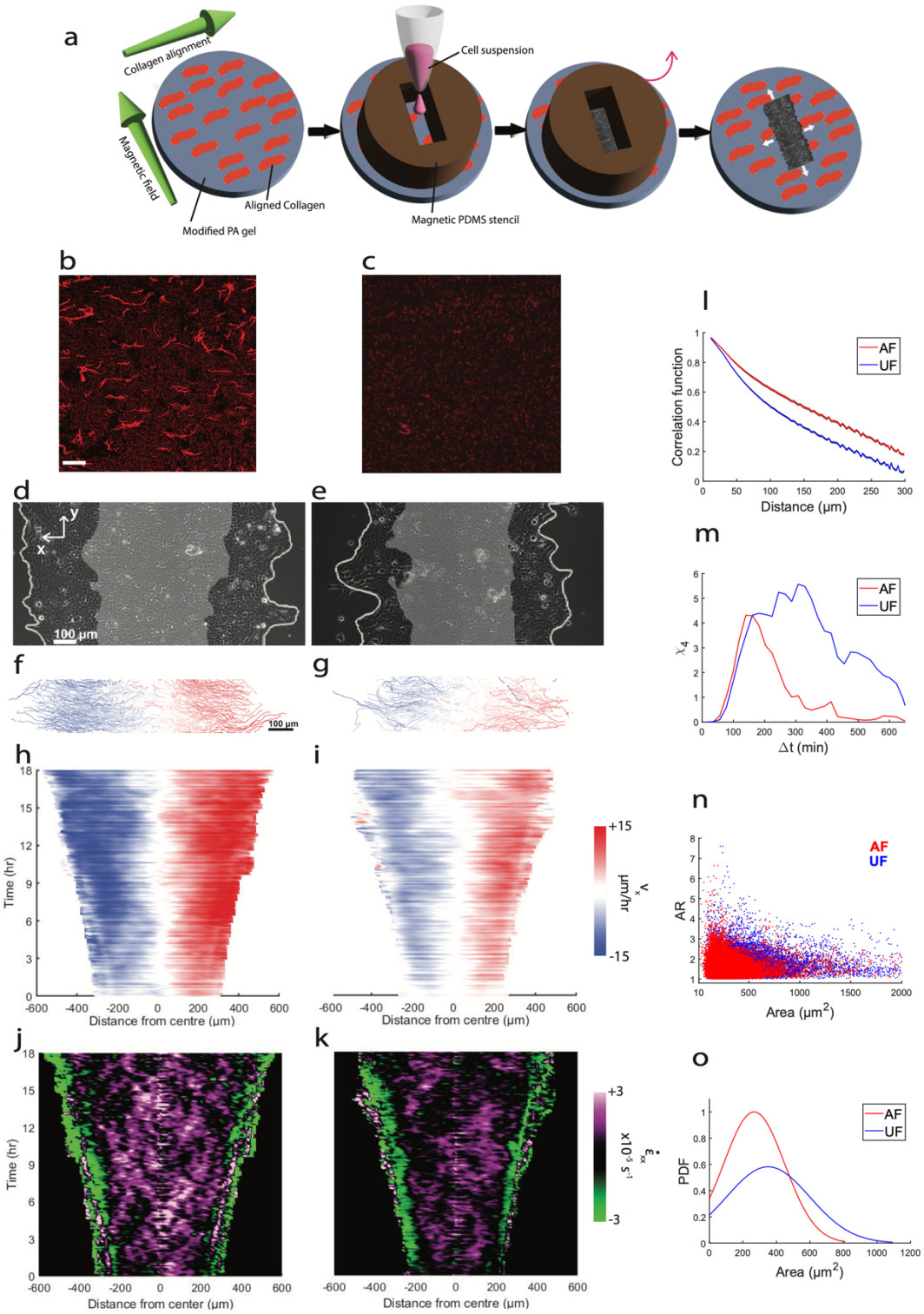

Figure 1. Aligned fibers cause faster and more directed motion within cell clusters. (**a**) Modified soft polyacrylamide (mod-PA) gels are exposed to high strength magnetic field to orient collagen in particular

direction. A PDMS stencil is deposited on the mod-PA gel. MCF-10A cells are seeded and allowed to attach only by the gap defined by PDMS stencil. When cells reach confluency, stencil is lifted, and cells start invading available space. Representative images of fluorescently labelled collagen-1 on AF (**b**) and UF (**c**). Scale bar is 50 µm. (**d**) A representative monolayer expanding on aligned fiber gels (AF). Gray transparent region indicates monolayer's initial position (t = 0 hours). Phase contrast shows the monolayer at 16hours. Gray lines indicate monolayer edges. (**e**) Example of monolayer expanding on uniform fiber gels (UF). (**f** and **g**) Individual cell trajectories corresponding to experiments shown in (d) and (e) respectively. Color-coding shows mean cell speed in x-direction for every track. Kymographs of cell velocity component in x-direction (v_x) (**h** and **i**), velocity strain rate $\dot{\varepsilon}_x$ (**j** and **k**) corresponding to experiments shown in (d) and (e) respectively. (**l**) Time-averaged (m = 157) spatial autocorrelation function of v_x for AF (red) and UF (blue) for n = 3 observations, error is represented as standard error. (**m**) The four-point susceptibility χ_4 as a function of Δt for AF (red) and UF (blue). (**n**) Scatter plots of cell aspect ratio (AR) versus cellular area for AF (56117 cells, red) and UF (39447 cells, blue). (**o**) Distribution of cellular area for cells on AF (red) and UF (blue).

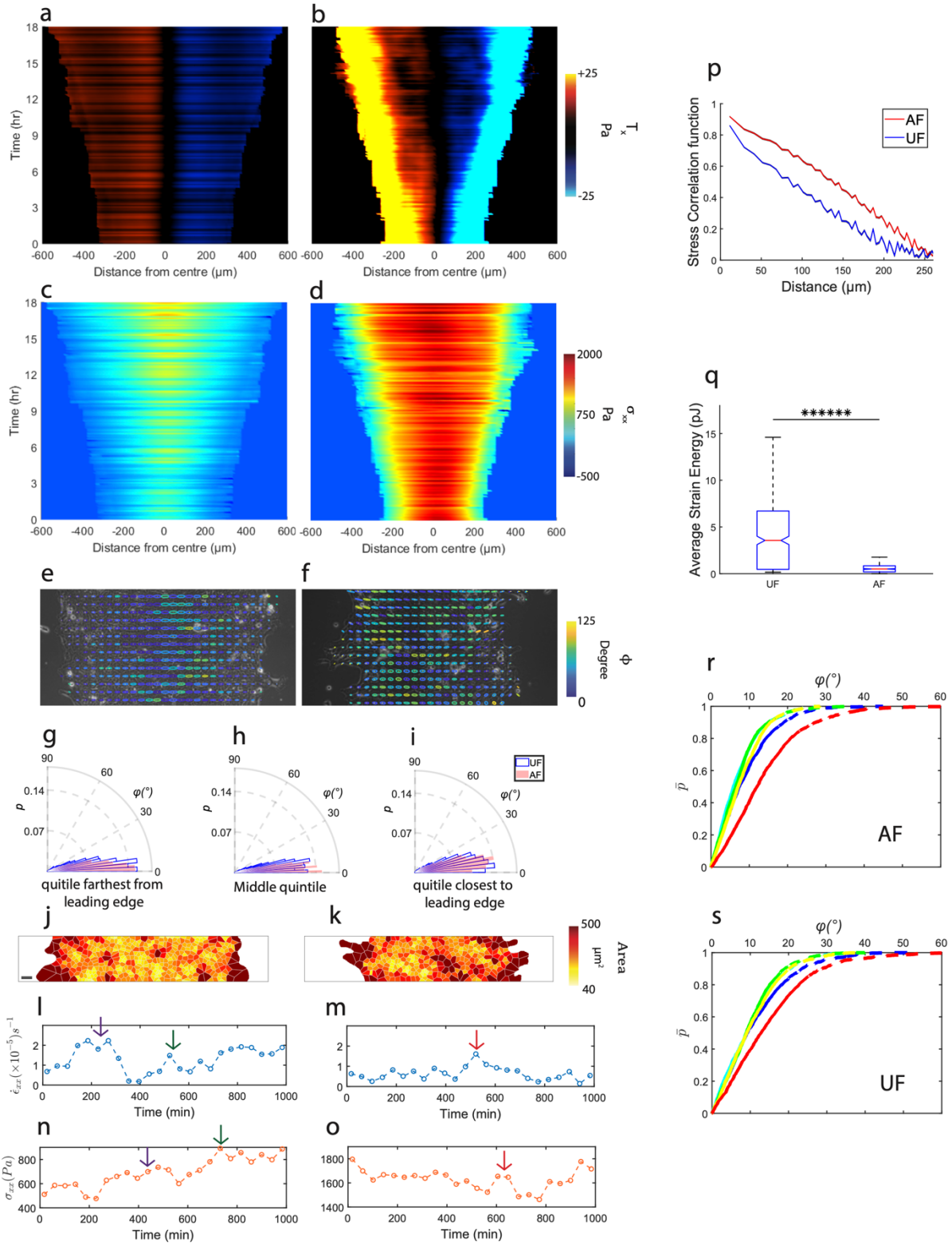

Figure 2. Aligned fibers reduces traction forces and monolayer stresses within migrating cell clusters causing a force effective mode of migration. (**a** and **b**) Kymographs for traction component T_x for AF (a)

and UF (b). (**c** and **d**) Kymographs for monolayer stress component σ_{xx}. (**e** and **f**) Principal stress ellipse overlaid on phase contrast images for monolayer on AF (e) and UF (f). Stress ellipse are color coded according to alignment angle φ between major axis of principle stress ellipse and direction of cellular velocity. (**g**-**i**) Alignment angle φ comparison between AF and UF at quintiles farthest (g), mid-distance (h) and closest (i) to the leading edge. In all three cases, distribution is narrower for AF indicating that "plithotaxis" is more dominant in AF compared to UF. (**j** and **k**) Polygons approximating cell shapes for monolayer on AF (j) and UF (k). Polygons are color coded corresponding to area. (**l** and **m**) Average value of $\dot{\varepsilon}_{xx}$ for AF (**l**) and UF (**m**) and σ_{xx} for AF (**n**) and UF (**o**). For curves in (l),(m),(n) and (o), four consecutive values were averaged for curve smoothening purposes. (**p**) Time averaged (m = 157) spatial correlation function of average-normal stresses in AF (red) and UF (blue) for n = 3 observations, error is represented as standard error. (**q**) Strain energy imparted by monolayer on AF and UF averaged across entire duration of migration (m = 157) across n = 3 (***** P = 1.98 x 10^{-84}). (**r**) Cumulative probability distribution $\bar{P}(\varphi)$ curves, from red to blue are at decreasing distance from leading edge for monolayer migrating on AF. (**s**) Cumulative probability distribution for monolayer migrating on UF. Each curve in (**r**) and (**s**) and distribution in (g), (h) and (i) have more than 1000 values.

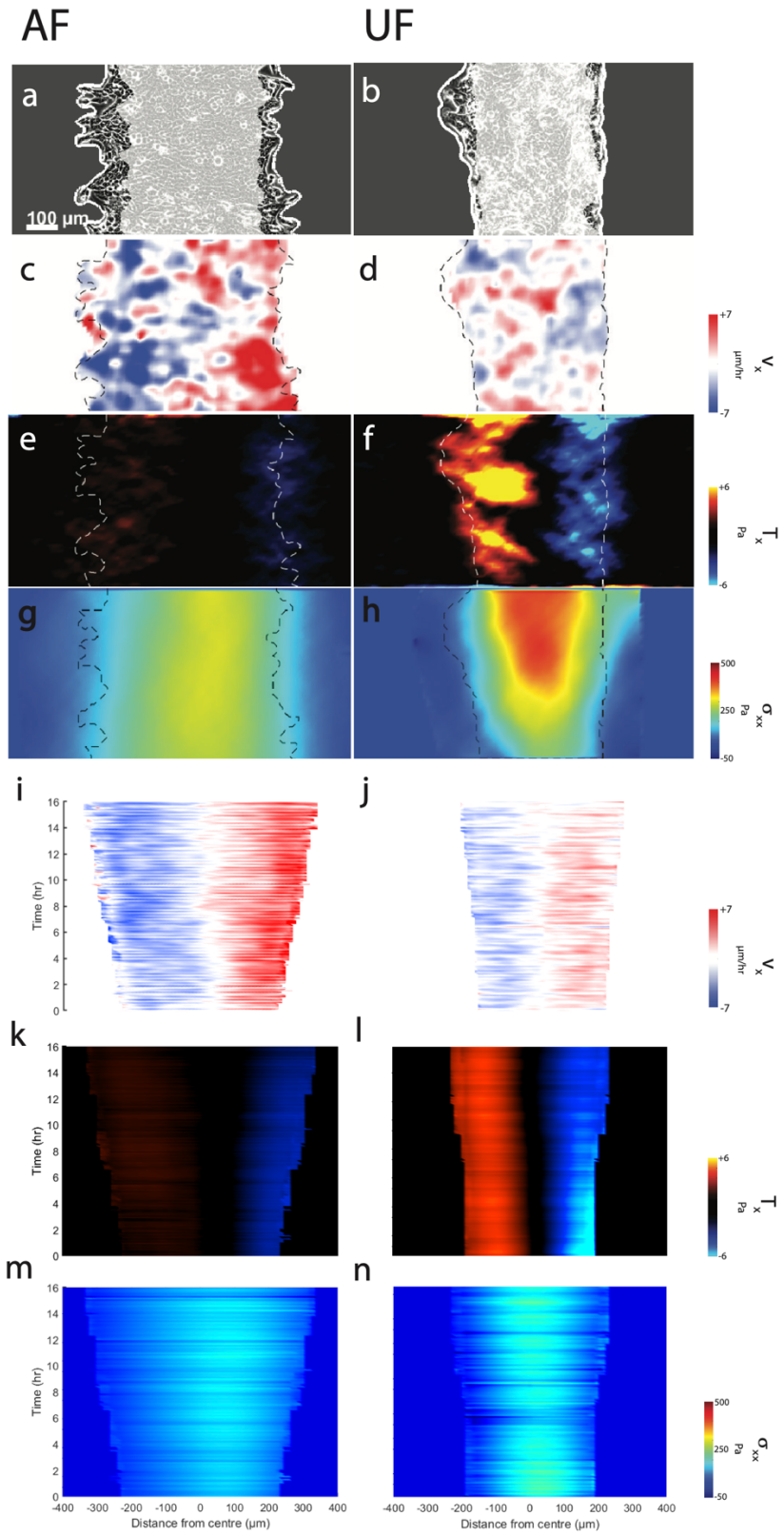

Figure 3. Reducing substrate stiffness maintains faster force effective migration phenotype on AF when compared to UF. (**a** and **b**) Phase contrast images of cell monolayer migrating of softer AF (a) and

softer UF (b). (**c** and **d**) Maps of velocity component v_x. (**e** and **f**) Maps of traction component T_x. (**g** and **h**) Maps of monolayer stress component σ_{xx}. (**i** and **j**) Kymographs of velocity component v_x for cell monolayer migrating of softer AF (a) and softer UF (b). (**k** and **l**) Kymographs of traction component T_x. (**m** and **n**) Kymographs of monolayer stress component σ_{xx}.

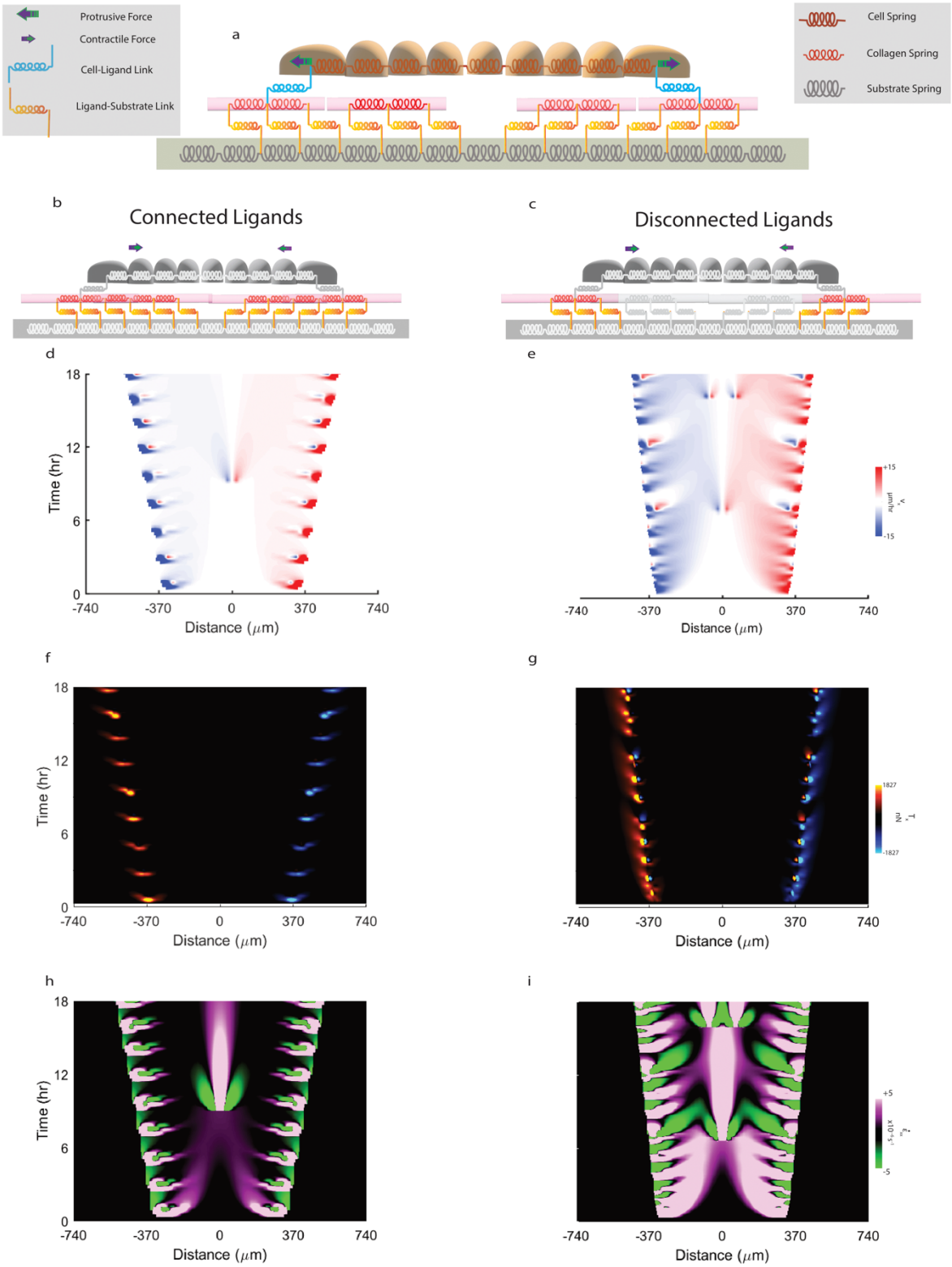
Protrusive Force
Contractile Force
Cell-Ligand Link
Ligand-Substrate Link
a
Cell Spring
Collagen Spring
Substrate Spring
b
Connected Ligands
c
Disconnected Ligands
d
e
f
g
h
i
Time (hr)
Distance (μm)
-740
-370
0
370
740
18
12
6
0

355

Figure 4. Physical model shows that fiber connectivity leads to rapid contractility stabilization leading to fast force-effective migration mode (**a**) Schematic of one-dimensional in-silico model of a line of epithelial cells represented by springs sliding viscously over rigid ligand springs which are fixed to substrate springs after a self-propelling force is acted upon at the leader nodes. (**b**) and (**c**) represent how connected ligands and disconnected ligands are modelled in-silico. In connected ligand condition (b), higher number of ligand-substrate bonds get engaged during contractility driven retraction of monolayer compared to disconnected condition (c). (**d** and **e**) In-silico velocity kymograph for connected ligands (d) and disconnected ligands (e). (**f** and **g**) In-silico traction force kymograph for connected ligands (f) and disconnected ligands (g). (**h** and **i**) In-silico strain-rate kymograph for connected ligands (h) and disconnected ligands (i).

Supplementary Information

Materials and Methods

Cell culture. MCF10A cells (Tissue Culture Support Center, Washington University, St Louis, USA) were cultured in DMEM/F12 (Invitrogen) supplemented with 5% (v/v) horse serum (Invitrogen), 20 ng/ml epidermal growth factor (EGF, Miltenyi Biotec Inc), 0.5 mg/ml hydrocortisone (Sigma-Aldrich), 100 ng/ml cholera toxin (Sigma-Aldrich), 10 µl/ml insulin (Sigma-Aldrich) and 1% (v/v) penicillin-streptomycin (Sigma-Aldrich).

Microfabrication of magnetic PDMS stencils. Cell monolayer was confined to a particular geometry by depositing magnetic PDMS stencil with a rectangular opening (500 µm) over the gel (*1*). Briefly, a mixture of PDMS and magnetite (25% w/w) was added to a mold which was 3D printed (Proto Labs Inc.). The mold containing PDMS mixture was kept in an oven to bake at 80° C. A magnet was attached to the bottom of the well plate just below the PA gels so that it can secure the magnetic PDMS stencil on top of the wet PA gel.

Fabrication of mod–PA hydrogels. Polyacrylamide (PA) gels were chemically modified by a method previously described in (*2*). Briefly, N-hydroxyethyl acrylamide (HEA) was oxidized to its primary aldehyde group N-ethanal acrylamide (EA) using pyridinium chlorochromate (PCC). The crude oxidized product was first purified via vacuum filtration to remove larger impurities and further purified by column chromatography using silica as solid phase and Ethyl Acetate as the mobile phase. Briefly, crude product was dissolved in Chloroform before running it through the column to separate product which was obtained as a white flakey solid upon evaporating excess solvent in a rota-evaporator (Buchi). Fourier-transform infrared spectroscopy (FTIR) was performed to confirm presence of aldehyde group in the purified product (Fig. S1c).

The synthesized EA was then incorporated into PA to facilitate protein conjugation. Modified Polyacrylamide gels of desired stiffness were prepared on glass-bottom 6 well-plates (Cellvis). Precursor PA solution was prepared by mixing acrylamide (A, Bio-Rad), EA and bis-acrylamide (B, Bio-Rad) (2.8% A:2.8% EA: 0.44% B) to result in 2.4 kPa stiffness gels as reported previously (*2*). Softer gels were synthesized using recipe (4.592% A:1.0% EA, 0.44% B) to result in approximate stiffness of 0.3 kPa. Polymerization was initiated by adding 0.5% ammonium persulfate (APS, Sigma-Aldrich) and 0.05% tetramethylethylenediamine (TEMED, Sigma-Aldrich) to the precursor mixture. Then, 60 µL of the precursor solution is sandwiched between a hydrophobic cover slip treated with Sigmacote (Millipore) and the silanized glass bottom 6 well plates. Next, the solution was allowed to polymerize in a vacuum chamber for 45 mins.

Magnetic alignment of Collagen-1. The modified PA gels were then incubated in 0.1 mg ml^{-1} type 1 collagen (rat tail collagen, Santa Cruz Biotechnology) inside the bore of a horizontal bore electromagnet for 2 hours at 4 C while fibillogenesis took place. Field strength for the magnet was 11 T. Collagen fibrils aligned at an angle of 90° to the direction of magnetic field due to presence of a positive diamagnetic anisotropy of the growing collagen fibrils (*3*)(*4*). The aligned fibrils deposited onto the gel and formed covalent linkages with the modified PA gel as described previously (*2*).

For gels with uniform collagen deposition, modified PA gels were incubated with 0.1 mg ml^{-1} type 1 collagen at 37 C for 1 h.

Fluorescent labelling of collagen and imaging. Collagen was fluorescently labelled according to method described in (*5*). Briefly, 1.5 ml of a 3 mg/ml collagen 1 solution (pH ~7.5) was gelled at 37°C inside a 12 multiwell plate and incubated with 0.2 M sodium bicarbonate buffer (pH 9.0, Sigma-Aldrich) for 10 min. Next, gel was incubated in 500 µl of Sulfo-Cyanine5 NHS ester dye (Lumiprobe Co. USA) solution (in DMSO) at room temperature in dark for 1 h. Remaining NHS ester was quenched by adding 3 ml of 50 mM Tris-HCL buffer (pH 7.5, Sigma-Aldrich). Later, stained collagen gel was washed with PBS 6 time over a period of 2 h. Afterwards, labelled gel was solubilized using 200 mM HCl (Sigma-Aldrich). The solubilized collagen solution was dialyzed against 20 mM acetic acid (Sigma-Aldrich) at a 1:1000 ratio with continuous stirring at 4°C for 4 h. Working collagen solution was prepared by replacing 4% of the unlabeled collagen solution with its labelled counterpart. Collagen coated hydrogels were imaged using Zeiss LSM 880 laser confocal microscope (Carl Zeiss Microscopy, Germany).

Cell monolayer patterning on soft hydrogels. Prior to using PDMS stencils for patterning, they were stored in 70 % ethanol overnight. To prevent cell and ligand adhesion to PDMS, stencils were then passivated by incubating them in 2 % Pluronic F-127 (Sigma-Aldrich) dissolved in PBS for 1 h. During the same time, gels which were coated with collagen are washed twice in PBS and incubated with media at 37° C. Magnets were attached to the bottom of the glass bottom dishes just below the hydrogels. Passivated PDMS stencils were washed twice in PBS and air dried for 20 min, and then were deposited on the surface of the hydrogels. Next, 100 µl of media containing 60,000 cells was added into the exposed region of the hydrogel and kept inside incubator for the cells to attach. After 1 h, unattached cells were washed away and 100 µl of fresh media was added. Twelve hours after seeding, cells reached desired cell density and stencils were carefully removed using tweezers and 3 ml of fresh media was added onto the wells.

Time-lapse microscopy. Migrating cells were imaged using Zeiss AxioObserver Z1 microscope (Carl Zeiss Microscopy) fitted with incubation. Cells were imaged after a 7 min interval over a period of 20 h using a 10x objective. Cells were allowed to acclimatize to the microscope incubation for 3 h before beginning image acquisition. Experiments were conducted in 37° C and 5% CO_2.To include the entire width of the monolayer, two images with 10% overlap were captured and then stitched using Zeiss stitching tool.

Cell velocities and trajectories. Velocity fields for migrating cells were computed via particle image velocimetry (PIV) though PIVlab package in MATLAB (*6*). Source code was modified to include a two-dimensional Hanning window across the interrogation window to improve PIV resolution and preventing boundary artifacts during cross-correlation. Velocity field (v_{ij}) was obtained by running PIV for three passes of 64-, 32- and 16- pixel windows. Monolayer boundaries were computed using home-built MATLAB script. Cell trajectories were obtained by tracking labelled cell nuclei using Fiji plugin TrackMate. Cell trajectories were imported in MATLAB and further analyzed using custom written scripts. Average cellular persistence in motion was measured as $\bar{p} = \langle \frac{L_{i,e}}{L_{i,c}} \rangle$, where $L_{i,e}$ is Euclidean distance covered by the cell i and $L_{i,c}$ is the contour length of its track. $\langle \ldots \rangle$ denotes average over all such tracks.

Quantifying dynamics of cellular motion. To quantify dynamics of cellular motion, we calculated the self-overlap order parameter (*7*).

$$Q(\Delta t) = N^{-1} \sum_{i=1}^{N} w_i$$

Where N is the number of cells, w = 1 if $|r_i(t+\Delta t) - r_i(t)| < 0.9 * d_c$ (where $r_i(t)$ is x-position of cell at time t and d_c is average cell diameter) and w = 0 otherwise. To measure the size and lifetime of the cooperative fluctuations within the migrating cluster of cells (*8*), the spatially heterogeneous dynamics in cellular motion was quantified by the four-point susceptibility χ_4, given by

$$\chi_4(\Delta t) = N[\langle Q(\Delta t)^2 \rangle - \langle Q(\Delta t) \rangle^2]$$

Where N is the number of cells, $\langle \ldots \rangle$ shows the average over sequence of images at all time, t. $\chi_4(\Delta t)$, is the four-point susceptibility and quantitatively shows the size of cooperatively motile cell clusters and their associated rearrangement times.

Fourier-transform traction microscopy. Traction forces were calculated from gel deformations which were recorded by measuring displacements in fluorescent marker beads (0.2 µm, mention vendor (??)) embedded inside the hydrogels on which cells were migrating. Displacements of the beads were measured in reference to the initial undisturbed condition obtained after trypsinization (10x) of cells. Bead strain field was calculated using PIV. This strain was then used to calculate the traction field by solving the inverse problem using a non-regularized Fourier transform algorithm previously employed in (*9*). Algorithm was implemented in MATLAB. The total energy U contribution from the monolayer towards the elastic distortion of the substrate was calculated by (*10*)

$$U = (\frac{1}{2}) \int \vec{T}(\vec{r}).\vec{u}(\vec{r}) dxdy$$

Monolayer stress microscopy. Stresses within the monolayer were calculated using monolayer stress microscopy implemented in MATLAB (*11*)(*12*). Finite element scheme was used to model cell monolayer, assumed to behave as thin sheet of uniform thickness (Poisson's ration 0.5, 5 µm height). Boundary conditions at the leading edge was assumed to be stress free. At the top and bottom optical edges, normal displacements and shear stresses were assumed to be zero ($u_i n_i = 0, \sigma_{ij} n_j t_i = 0$).

Spatial autocorrelation function of tension. Extent of spatial cell-cell coordination in terms of velocities and stresses was quantified by the spatial autocorrelation function (*13*)

$$C(R) = \frac{1}{N\mathrm{var}(\bar{\sigma})} \sum_{i,j=1}^{N} \left[\sum_{|R_i - R_j| = R} \delta\bar{\sigma}_i \delta\,\bar{\sigma}_i \right]$$

$\delta\bar{\sigma}_i$ is local departure of tension at position R_i from the spatial mean $\langle\sigma\rangle$, while $\mathrm{var}(\bar{\sigma})$ is the variance of those departures, and $|R_i - R_j| = R$ denotes the bin width which consists of N points. We used the same function to quantify the spatial coordination of velocity vectors. Plots were generated by averaging 4 consecutive values for smoothening purposes.

Kymographs. Every pixel's position within the monolayer was computed from the nearest leading edge. Next, we calculated mean values of velocities, velocity strain rates, tractions and monolayer stresses of all pixels at a given distance from leading edge. These values were then represented as a single

dimension segment of the monolayer for a single time point. These segments were obtained for every time point and staked together to result in the kymographs

Quantifying cell shapes. 900 cells for AF and 600 cells for UF were manually tracked by annotating their nuclei using MATLAB image labelling app. Labelled cell nuclei were then used to generate a voronoi tessellation to approximate cellular boundaries. These boundaries were used to approximate area of cells. The cell's aspect ratio (AR) was then computed from the ratio of second area moments of I for the polygon (*14*). Codes were implemented in MATLAB.

$$I = \begin{bmatrix} \int x^2 dA & \int xydA \\ \int xydA & \int y^2 dA \end{bmatrix},\ AR \equiv \sqrt{\frac{I_1}{I_2}}$$

Statistical analysis. Statistical testing is done using two-sample t-test. In figures, m represents total number of time steps that were analyzed and n represents total number of observations. Wherever n is not mentioned, it indicates one representative video. Statistical test was done using MATLAB.

One-dimensional motor-clutch model of monolayer expansion

Overview. As shown in (Fig. 4a), the model is composed of cell monolayer, substrate and an intermediate layer of ligand which connects monolayer to substrate. Each of these layers is modelled as a collection of springs connected in series. Connector springs between cell monolayer and ligand springs depict adhesion complexes represented by various proteins like integrin, paxillin, vinculin and talin which bind actin to extra-cellular matrix proteins (*15*) represented here by the ligand layer. The ligand layer is attached to the underlying substrate via links which represent the covalent attachment between collagen fibers and mod-PA gels in experiments. Additionally, the protrusive part of the monolayer is represented by protrusive nodes at each end of the cell layer which is acted upon by a constant force F_p. Force is transmitted across cell-cell junctions and to the substrate via intermediate ligand layer from the monolayer edges (*16*). Next, we summarize the different components of the model and also its numerical implementation.

Cell monolayer. Monolayer is modelled as a collection of springs connected in series. While protrusions are implemented only at the leading edge, cellular contractility which has been modelled as variable within monolayer depths previously (*17*) has been modelled by modulating the stiffness of connected springs. Stiffness of the connecting springs follows a normal distribution such that springs at the leading edge are stiffer than springs at the center (Fig. S5a). Since leader springs are responsible for generating protrusions, it thus implies that their contractility should be higher such that the resulting contraction after a protrusion event can be translated into sufficient pulling force for the following cells. Moreover, recent experiments have also shown leader cells to have much higher stiffness compared to follower cells (*18*)As a result, the spring stiffness have the following stiffness.

$$k_c(x_c) = ndfactor(maxStiffness + minStiffness - \frac{1}{\sigma_k\sqrt{2\pi}} e^{-\frac{1}{2}\left(\frac{x_c-\mu_k}{\sigma_k}\right)^2})$$

We implemented monolayer fluidization by splitting cells into two when they undergo stretching beyond a threshold length. Epithelial would healing studies have shown that leading edge is non proliferative and

involved in active migration by lamellipodia formations leading to cell stretching (*19*) while follower cells consist of the proliferation hub responsible for supplying new cells (*20*)(*21*)(*22*) Since in our experiments, there are two wound edges to the left and right, we assume that the proliferation band is the middle of the monolayer. We thus use a strain threshold length which also follows a normal distribution with respect to distance from leading edge (Fig. S5b), where cells at the two leading edge have least capacity to divide while cells at center have highest capacity to divide.

$$\varepsilon_c_{th}(x) = maxTDL + \ (ndfactor) * (minND - \frac{1}{\sigma_\varepsilon\sqrt{2\pi}} e^{-\frac{1}{2}(\frac{x_c-\mu_\varepsilon}{\sigma_\varepsilon})^2})$$

Since we make sure that cell division is more prevalent in the middle of monolayer than near the leading edge, consequently we also varied the friction each node experiences according to its distance from the monolayer center following a normal distribution (Fig. S5c). We argue that cell crowding occurs at the center leading to higher friction leading to contact inhibition of motion compared to leading edges where there are more open spaces and lesser cellular densities. Thus to capture 2-D contact inhibition in 1-D, the damping constant follows the below equation

$$\eta_c(x) = minDC + ndfactor(\frac{1}{\sigma_\eta\sqrt{2\pi}} e^{-\frac{1}{2}\left(\frac{x_c-\mu_\eta}{\sigma_\eta}\right)^2} - minND)$$

Ligand layer. We implemented aligned fibers in the 1-d by joining multiple nodes in series to form connected fiber. Uniform fibers were modelled as disconnected fibers with every two nodes disconnected from the third node leading to discontinuity in ligand connectivity (Fig. 4b,c). Every ligand node is connected to substrate node via springs representing covalent linkages between collagen fiber and mod-PA gel.

Substrate layer.

Substrate is modelled as a series of springs connecting substrate nodes and have uniform stiffness.

Model implementation. Force balance at every cell node x_c_i reads (1), where F_{c-c} represents force at cell-cell junction and F_{c-l} represents force at cell-cell junction. F_p represents protrusive force which only acts first node and last node ($i = 1\ OR\ i = N$). Here, ε_c_i denotes strain experienced by spring connecting nodes x_c_i and x_c_{i+1}, and $\dot{x_c_i}$ denotes velocity of node x_c_i.

$$F_p + F_{c-c} + F_{c-l} + k_c\varepsilon_i - k_c\varepsilon_c_{i+1} - \ \eta_c\dot{x_c_i} = 0 \qquad (1)$$

Force balance at every ligand node x_l_i reads (2), where F_{l-l} represents force at ligand-ligand spring junction and F_{l-s} represents force at ligand-substrate spring junction.

$$F_{l-l} - F_{c-l} + F_{l-s} + k_l\varepsilon_l_i - k_l\varepsilon_l_{i+1} - \ \eta_l\dot{x_l_i} = 0 \qquad (2)$$

Force balance at every ligand node x_i reads (3), where F_{s-s} represents force at substrate-substrate spring junction.

$$F_{s-s} - F_{l-s} + k_s\varepsilon_s_i - k_s\varepsilon_s_{i+1} - \ \eta_s\dot{x_s_i} = 0 \qquad (3)$$

For each incremental time step, the following algorithm is implemented:

1. Apply protrusive motor force to leader node only if it is at equilibrium.
2. Solve equation 1 for nodes representing the cell mesh.
3. Solve equation 2 for nodes representing the ligand mesh.
4. Solve equation 3 for nodes representing the substrate mesh.
5. Displaced leader node attaches to the nearest ligand node engaging clutch.

Computational simulations were numerical implemented using a forward Euler method. All equations were implemented in a C++ code developed by the author. Multiple class definitions were borrowed from CHASTE library (*23*) an online code repository for cell based simulations.***Simulation parameters.***

We used spring constant values of $k_{collagen} = 685\ \mu N$, $k_{substrate} = 228\ \mu N$, $k_{cell-collagen\ link} = 1142\ \mu N$, $k_{substrate-collagen\ link} = 456\ \mu N$. We applied protrusive force of $F_p = 3083\ \mu N$ on leader nodes. We also used damping constant values of $\mu_{collagen} = 0.22\ kgs^{-1}$, $\mu_{substrate} = 0.22\ kgs^{-1}$.

Supplementary Figures:

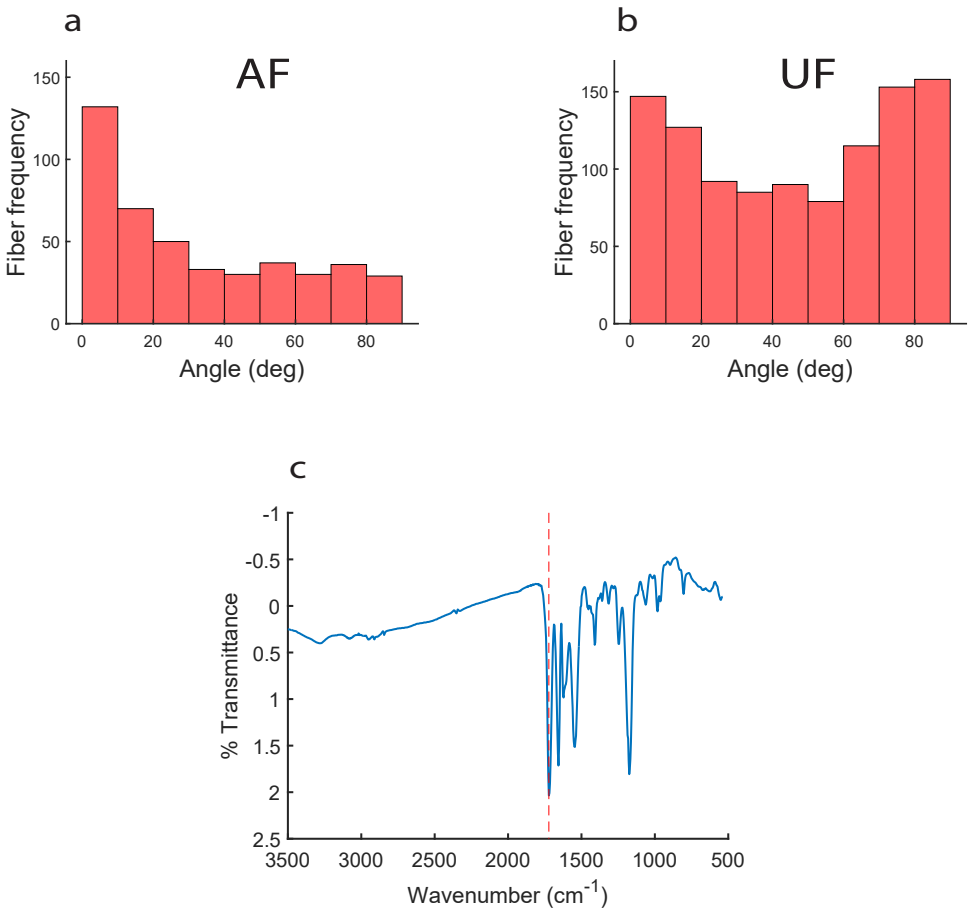

Figure S1. (**a** and **b**) Histogram depicting orientation angle distribution for collagen fibrils on AF (a) and UF (b). (**c**) FTIR plot showing presence of aldehyde group peak at 1722 cm^{-1}. More than 400 fibers were analyzed for plots in **a** and **b**.

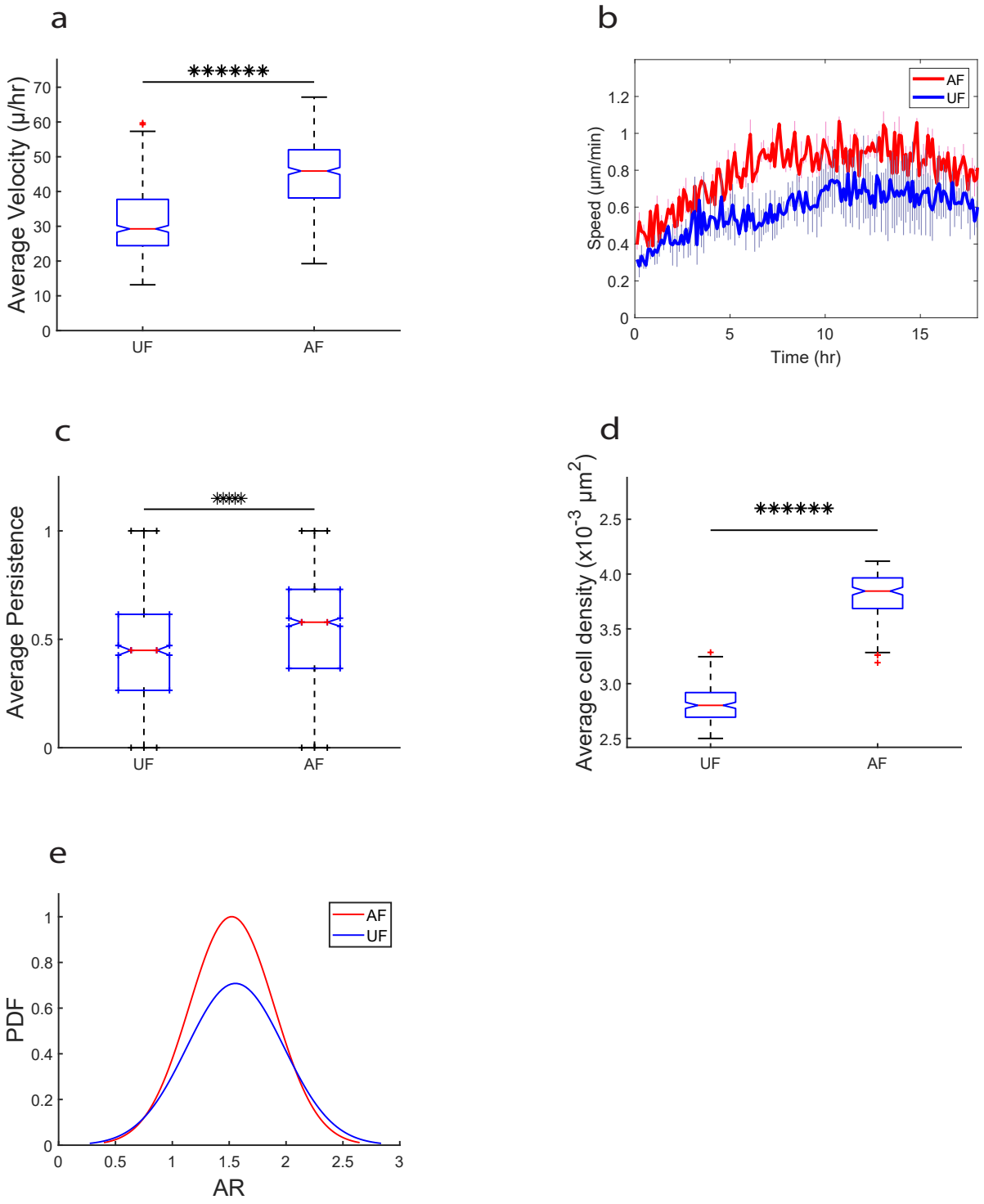

Figure S2. (**a**)Box-plot comparison of average velocity comparison for cells migrating on AF and UF (m = 157, n = 3, p = 1.98 x 10^{-84}). (**b**) Average velocity of cells migrating on AF and UF as a function of time. Error is represented as standard error (m = 157, n = 3). (**c**) Time averaged cellular persistence over the entire duration of experiment (900 tracks for AF, 500 tracks for UF, p = 5 x 10^{-18}). (**d**) Time average (m = 158) cellular density comparison for cells on AF and UF (p = 1.8 x 10^{-127}). (**e**) Distribution of cellular aspect rations for cells on AF (red) and UF (blue).

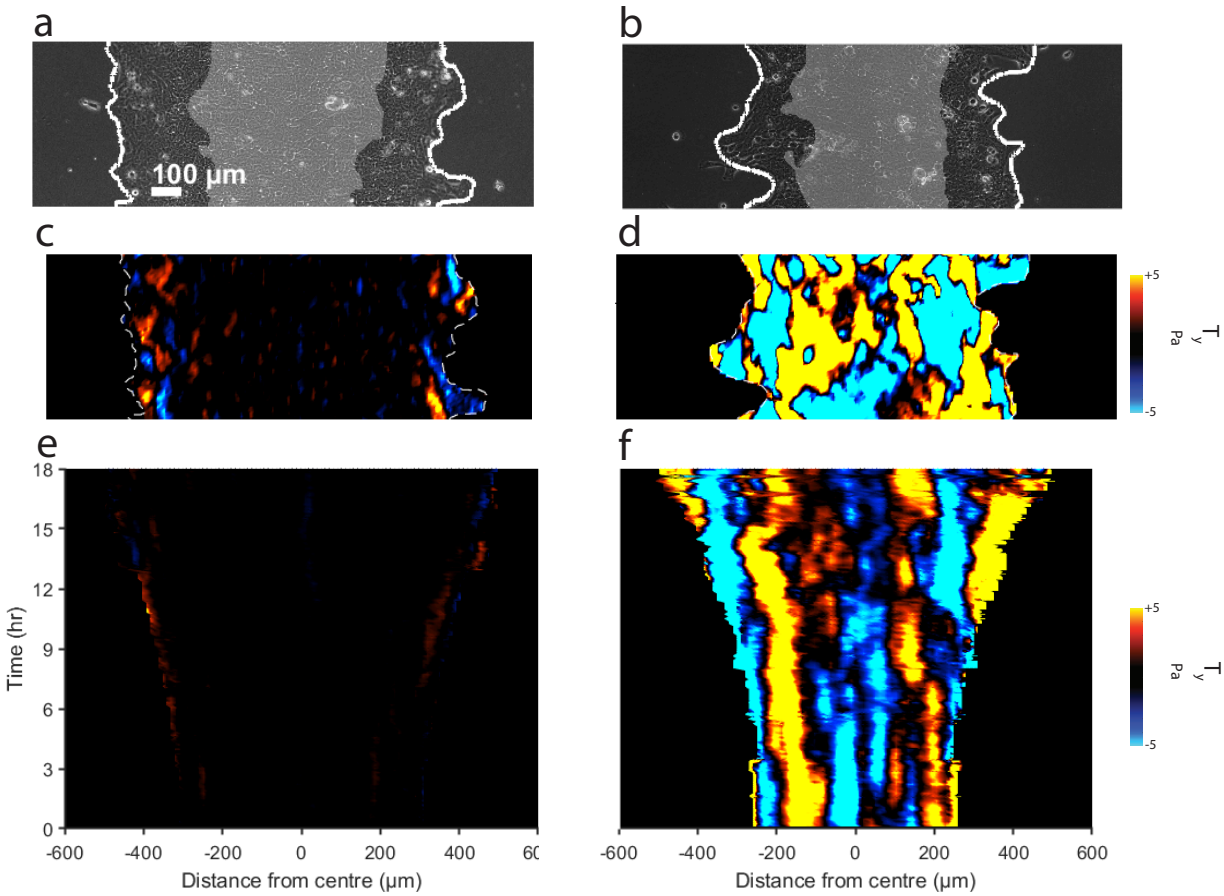

Figure S3. (**a** and **b**) Phase contrast images of cell monolayer migrating of AF (a) and UF (b). (**c** and **d**) Maps of traction component T_y. (**e** and **f**) Kymographs for T_y.

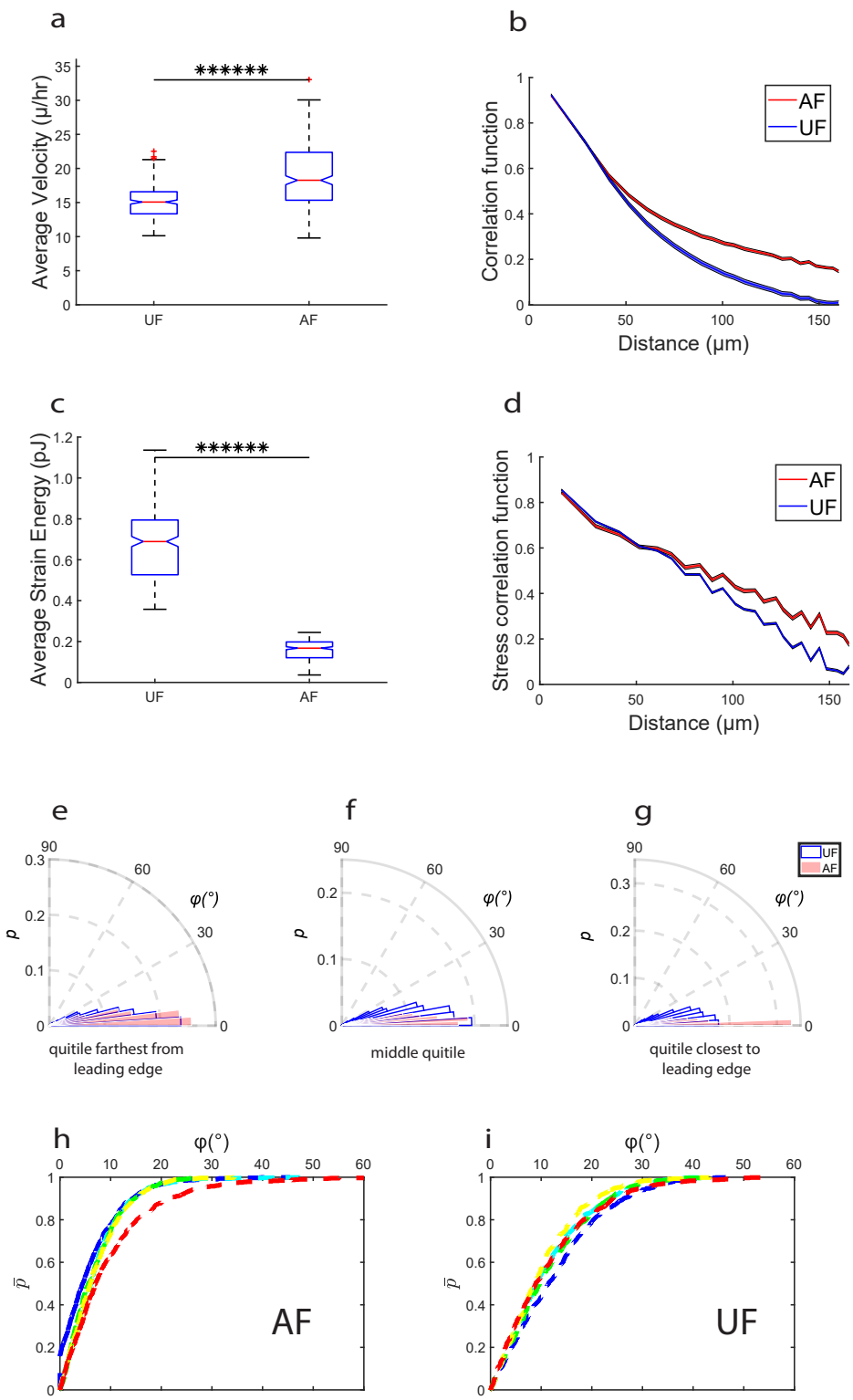

Figure S4. (**a**)Box-plot comparison of average velocity comparison for cells migrating on AF and UF (m = 146, n = 2, p = 1.40 x 10^{-28}). (**b**) Time-averaged spatial autocorrelation function of v_x for AF (red) and UF (blue), error is represented as standard error. (**c**) Strain energy imparted by monolayer on AF and UF averaged across entire duration of migration (m = 146, n = 2, p = 6.43 x 10^{-222}). (**d**) Time averaged (m =

157) spatial correlation function of average-normal stresses in AF (red) and UF (blue), error is represented as standard error for n = 2 observations. (**e**-**g**) The alignment angle φ comparison between AF and UF at quintiles furthest (e), mid-distance (f) and closest (g) to the leading edge. In all three cases, distribution is narrower for AF indicating Plithotaxis is more dominant in AF compared to UF. (**h**) Cumulative probability distribution $\bar{P}(\varphi)$ curves, from red to blue are at decreasing distance from leading edge for monolayer migrating on AF. (**i**) Cumulative probability distribution for monolayer migrating on UF.

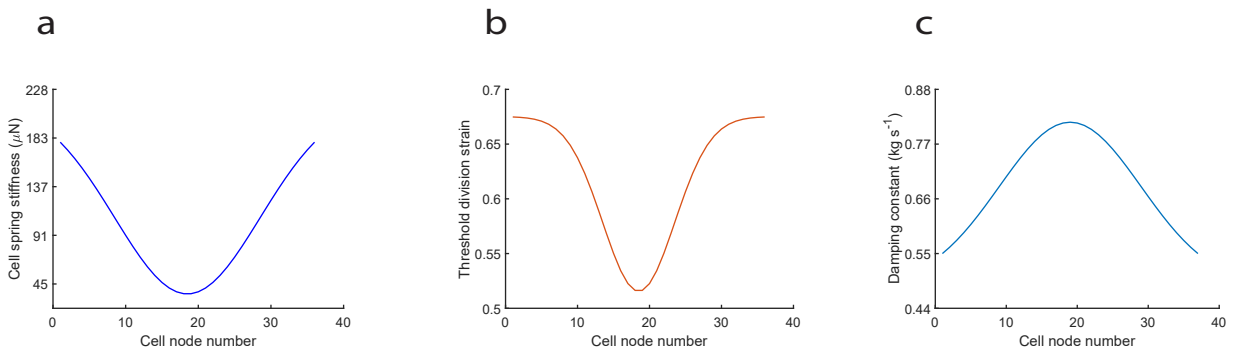

Figure S5. (**a**) Plot showing variation in cell spring stiffness across the cell nodes in-silico. (b) Plot showing variation in threshold division strain across the cell nodes in-silico. (**c**) Plot showing variation in damping constant across cell nodes in-silico.

References

1. M. Poujade *et al.*, Collective migration of an epithelial monolayer in response to a model wound. *Proc. Natl. Acad. Sci.* ***104***, 15988–15993 (2007).

2. B. Sarker, A. Bagchi, C. Walter, J. Almeida, A. Pathak, Longer collagen fibers trigger multicellular streaming on soft substrates via enhanced forces and cell–cell cooperation. *J. Cell Sci.* ***132***, jcs226753 (2019).

3. J. Torbet, J.-M. Freyssinet, G. Hudry-Clergeon, Oriented fibrin gels formed by polymerization in strong magnetic fields. *Nature*. ***289***, 91–93 (1981).

4. G. Hudry-Clergeon, J. M. Freyssinet, J. Torbet, J. Marx, Orientation of fibrin in strong magnetic fields. *Ann. N. Y. Acad. Sci.* ***408***, 380–387 (1983).

5. A. D. Doyle, N. Carvajal, A. Jin, K. Matsumoto, K. M. Yamada, Local 3D matrix microenvironment regulates cell migration through spatiotemporal dynamics of contractility-dependent adhesions. *Nat. Commun.* ***6***, 8720 (2015).

6. W. Thielicke, R. Sonntag, PIVlab – towards user-friendly, affordable and accurate digital particle image velocimetry in MATLAB. *J. Open Res. Softw.* (2014) [Online]. Available: https://openresearchsoftware.metajnl.com/articles/10.5334/jors.bl/#.

7. A. R. Abate, D. J. Durian, Topological persistence and dynamical heterogeneities near jamming. *Phys. Rev. E*. ***76***, 21306 (2007).

8. B. L. *et al.*, Direct Experimental Evidence of a Growing Length Scale Accompanying the Glass Transition. *Science (80-.).* ***310***, 1797–1800 (2005).

9. X. Trepat *et al.*, Physical forces during collective cell migration. *Nat. Phys.* ***5***, 426–430 (2009).

10. J. P. Butler, I. M. Tolić-Nørrelykke, B. Fabry, J. J. Fredberg, Traction fields, moments, and strain energy that cells exert on their surroundings. *Am. J. Physiol. Cell Physiol.* ***282***, C595-605 (2002).

11. D. T. Tambe *et al.*, Collective cell guidance by cooperative intercellular forces. *Nat. Mater.* ***10***, 469–475 (2011).

12. A. Saraswathibhatla, E. E. Galles, J. Notbohm, Spatiotemporal force and motion in collective cell migration. *Sci. Data*. ***7***, 197 (2020).

13. D. T. Tambe *et al.*, Collective cell guidance by cooperative intercellular forces. *Nat. Mater.* ***10***, 469–475 (2011).

14. L. Atia *et al.*, Geometric constraints during epithelial jamming. *Nat. Phys.* ***14***, 613–620 (2018).

15. C. Selhuber-Unkel, T. Erdmann, M. López-García, H. Kessler, U. S. Schwarz, J. P. Spatz, Cell adhesion strength is controlled by intermolecular spacing of adhesion receptors. *Biophys. J.* ***98***, 543–551 (2010).

16. R. Sunyer *et al.*, Collective cell durotaxis emerges from long-range intercellular force transmission. *Science (80-.).* ***353***, 1157–1161 (2016).

17. S. Banerjee, K. J. C. Utuje, M. C. Marchetti, Propagating Stress Waves During Epithelial Expansion. *Phys. Rev. Lett.* ***114***, 228101 (2015).

18. Y. L. Lee, J. Mathur, C. Walter, H. Zmuda, A. Pathak, Matrix obstructions cause multiscale disruption in collective epithelial migration by suppressing physical function of leader cells. *bioRxiv*. 2022.04.28.489943 (2022).

19. K. Safferling *et al.*, Wound healing revised: a novel reepithelialization mechanism revealed by in vitro and in silico models. *J. Cell Biol.* ***203***, 691–709 (2013).

20. K. A. U. Gonzales, E. Fuchs, Skin and Its Regenerative Powers: An Alliance between Stem Cells and Their Niche. *Dev. Cell*. ***43 4***, 387–401 (2017).

21. M. Ito *et al.*, Stem cells in the hair follicle bulge contribute to wound repair but not to homeostasis of the epidermis. *Nat. Med.* ***11***, 1351–1354 (2005).

22. V. Levy, C. Lindon, Y. Zheng, B. D. Harfe, B. A. Morgan, Epidermal stem cells arise from the hair follicle after wounding. *FASEB J. Off. Publ. Fed. Am. Soc. Exp. Biol.* ***21***, 1358–1366 (2007).

23. J. Pitt-Francis *et al.*, Chaste: A test-driven approach to software development for biological modelling. *Comput. Phys. Commun.* ***180***, 2452–2471 (2009).